Giant, 17, 2024, 100240

Full-length article

Tunable glycyrrhizic acid supramolecular hydrogels via metal ion complexation

Xinke Yu [a], Mengyue Xu [a,b], Jiyang Cai [a], Qing Li [a], Yunyi Yang [a], Zhili Wan [a,c,*], Xiaoquan Yang [a]

[a] Laboratory of Food Proteins and Colloids, School of Food Science and Engineering, Guangdong Province Key Laboratory for Green Processing of Natural Products and Product Safety, South China University of Technology, Guangzhou 510640, PR China
[b] Laboratory of Physics and Physical Chemistry of Foods, Wageningen University, Bornse Weilanden 9, 6708WG Wageningen, The Netherlands
[c] Overseas Expertise Introduction Center for Discipline Innovation of Food Nutrition and Human Health (111 Center), Guangzhou 510640, PR China

Keywords: Glycyrrhizic acid, Supramolecular hydrogels, Metal ion complexation, Large amplitude oscillation shear (LAOS), Lissajous-Bowditch curves, Gel networks

Glycyrrhizic acid (GA) is a natural edible chiral triterpene saponin that can undergo hierarchical self-assembly in water to form supramolecular hydrogels. Customizing the properties of GA supramolecular hydrogels is crucial for their wide food and biomedical applications, and the incorporation of specific metal ions can be an attractive way for this purpose. Herein, this study investigates the effects of metal ions with different valence states and concentrations on the linear and nonlinear rheological properties and network structures of GA supramolecular hydrogels. Monovalent metal ions (Na^+ and K^+), exhibiting weak binding affinity to GA, rely on the electrostatic screening effects at high concentrations (e.g., 50 mM) to enhance the GA interfibrillar interactions and thus the formation of a more compact and ordered gel network, which displays a pronounced nonlinear rheological behavior with a typical transition from elastic to viscous response. Polyvalent metal ions (Ca^{2+}, Zn^{2+}, and Al^{3+}), owing to their greater charge density and stronger binding with GA, significantly enhance the network strength of the hydrogels at low concentrations (e.g., 5 mM). Nonetheless, at high ion concentrations (e.g., 50 mM), the GA-M^{n+} forms discrete aggregated network structures due to excessively strong cation-carboxylate complexation, leading to the irregular nonlinear rheological responses and the lower resistance to large deformations. These findings can deepen our understanding of the highly tunable rheological behaviors and network structures of GA hydrogels, which demonstrates a new possibility for the design and development of responsive natural supramolecular hydrogels with controlled properties through the strategy of metal ion complexation.

1 Introduction

Supramolecular hydrogels, an eminent category of soft materials generally formed through the self-assembly of low molecular weight gelators (LMWGs) in aqueous solutions via non-covalent interactions like π-π stacking, hydrogen bonding, van der Waals forces, hydrophobic effects, and ion coordination, have garnered significant attention during the last few decades [1–7]. As a typical class of building blocks to construct supramolecular materials, LMWGs undergo a hierarchical self-assembly, leading to the formation of a range of well-defined nanostructures

* Corresponding author.
E-mail address: zhiliwan@scut.edu.cn (Z. Wan).
Received 17 November 2023; Received in revised form 10 January 2024; Accepted 11 January 2024

https://doi.org/10.1016/j.giant.2024.100240

such as nanofibrils, which further entangle to create a solid-like, three-dimensional gel network [8,9]. Compared with their synthetic counterparts, the naturally derived LMWGs that can self-assemble into supramolecular hydrogels offers many excellent properties, including the inherent bioactivity, biocompatibility, and biodegradability, which endow them with the immense potential as supramolecular hydrogelators with high safety and sustainability for diverse biomedical applications, such as drug delivery, wound healing, and tissue engineering [10–12].

Glycyrrhizic acid (GA) is an exquisite natural compound extracted from the root of the licorice plant, possessing a variety of biological activities, including anti-inflammation, hepatoprotective, anticancer, and antiviral activities [13–15]. From a chemical structure perspective, GA is classified as a chiral amphiphilic molecule, comprising a hydrophobic triterpenoid aglycon moiety known as 18β-glycyrrhetinic acid, conjoined with a hydrophilic diglucuronic unit. The intrinsic amphiphilicity and chirality of GA molecules bestow them with the propensity to undergo anisotropic self-assembly in water forming supramolecular nanofibrils via hydrophobic interactions of the triterpene fragments and hydrogen bonds of the glucuronic fragments [16]. The formed elongated semi-flexible GA nanofibrils, exhibiting a right-handed twist, with approximately 2.5 nm in width and a periodicity of 9 nm, can further entangle to form supramolecular hydrogels with a three-dimensional hydrogen-bonded fibrillar network [17]. Moreover, the presence of numerous functional groups, rigid frameworks, and distinctive stacking behaviors within the GA molecules provide them an ideal structural motif for generating a wide array of GA derivatives, facilitating the development of multifunctional hydrogel materials [18–21]. Interestingly, our investigations demonstrate the combined gelation and amphiphilic properties of GA fibrillar assemblies can render them the ability to serve as fundamental building blocks for creating novel structured multiphase colloidal materials, such as gel emulsions [22–24] and ultrastable gel foams [25–27]. Recently, the GA supramolecular hydrogels with versatile functional attributes find diverse applications in a variety of fields, such as targeted drug delivery vehicles [21,28], harnessing their specific stimuli-responsiveness, additive manufacturing [29], taking advantage of the injectability and thixotropic recovery, and wound healing or wearable biosensors [20,29], owing to their high bioactivity and modulable mechanical properties, self-healability, and adhesion. Considering the wide range of applications, it is desirable to understand and control the rheological properties of GA supramolecular hydrogels, since the rheological behaviors of a supramolecular gel play a critical role in determining its processing and functional performances in practical applications, and therefore, the modulation of gel rheology will be very important for meeting real requirements in various fields.

Generally, the rheological properties of supramolecular hydrogels can be tailored by adjusting the gel components including the concentration and molecular structure of gelators [30,31], and the attribute of the employed solvents [32]. Moreover, the use of external stimuli, for instance, variation of temperature and pH [33,34], addition of anions [35], and the incorporation of metal ions [36,37], allows an effective control of the rheological properties of supramolecular hydrogels. In recent years, there has been a growing interest in the incorporation of metal ions to finely tune the properties of supramolecular hydrogels, particularly their rheological characteristics [38–41]. For monovalent metal ions, Adams and co-workers discovered that Li^+, Na^+, and K^+ paired with 2-naphthylalanine-phenylalanine (Li-2NapFF, Na-2NapFF, and K-2NapFF) systems exhibited abrupt transitions in the viscoelastic moduli compared to Rb-2NapFF and Cs-2NapFF, indicating the significant differences in affecting the gel properties [39]. Barthélémy and co-workers found that with an increase in the concentration of Li^+, Na^+, and K^+, the rheological modulus values of nucleotide lipid hydrogels ($diC_{16}dT$) initially rose and then subsequently declined, and Li-$diC_{16}dT$, Na-$diC_{16}dT$, and K-$diC_{16}dT$ spontaneously assembled into supramolecular hydrogels via the formation of entangled fibers [40]. For polyvalent metal ions, Roy and co-workers showed that in the presence of Fe^{2+} and Mn^{2+}, the network strengths of functional peptides (Fmoc-HL-COOH) significantly decreased to 3.3 kPa and 5.1 kPa, respectively, as compared to that of only Fmoc-HL-COOH (11.5 kPa). However, with Cu^{2+} and Ni^{2+}, G′ was 15.4 kPa and 12.8 kPa respectively [41]. These studies reveal that the rheological properties of supramolecular hydrogels are largely affected by the addition of different types and valences of metal ions.

As a natural edible LMWG, GA is a polyprotic weak acid with three carboxylic groups that can dissociate in multiple steps, endowing it with the ability to form complexes with metal ions. Our previous study has shown that the addition of Na^+ significantly increased the viscoelastic moduli of GA supramolecular hydrogels, and a dramatic increase in turbidity of hydrogels can be observed with the increasing concentration of Na^+ [27]. These phenomena primarily stem from the elevation in ionic strength, which diminishes the electrostatic repulsion between GA molecules/nanofibrils, thereby promoting inter-fibrillar aggregation. Based on these findings, it is reasonable to postulate that the metal ions, especially those with varying valence states, can manipulate the self-assembly behavior of GA nanofibrils, which consequently impacts the rheological properties and microstructure of supramolecular hydrogels [42,43]. Thus, there is a need to systematically understand the influence of metal ions complexation on the structural properties of GA supramolecular hydrogels, with the aim of tuning the rheological behaviors of GA hydrogels through metal complexation for meeting the specific processing and application requirements. Herein, we select six common metal ions, spanning a range of valences from monovalent to trivalent, with the accompanying anions of all chloride ions, and aim to unravel the impact of these metal ions on the rheological and structural properties of GA supramolecular hydrogels. The small amplitude oscillatory shear (SAOS) experiments were first conducted to explore the linear viscoelastic properties of GA-metal ions complexation hydrogels (GA-M^{n+}). To acquire more in-depth information on the rheology of GA supramolecular hydrogels, the large amplitude oscillatory shear (LAOS) tests were then performed for nonlinear viscoelastic characterization. The combination of the Lissajous-Bowditch curves and the index of nonlinearity, which can provide valuable insights into the

nonlinear rheological responses, were further adopted to quantify the nonlinear viscoelasticity of the GA-M^{n+} hydrogels. The complexation mechanism between GA and metal ions was also elucidated by a series of microscopy and spectroscopy techniques and density-functional theory (DFT) calculations. The findings obtained in this work can contribute to a better understanding of the structure-rheology relationship of GA-M^{n+}, extending the real applications of GA supramolecular hydrogels.

2 Materials and methods

2.1 Materials

Glycyrrhizic acid mono ammonium salt (GA, purity >98%) was purchased from Thermo Fisher, USA. Sodium chloride, potassium chloride, calcium chloride, zinc chloride, aluminum chloride, and iron (III) chloride were bought from Chemical Reagent Co., Ltd. (China). Milli-Q water (18.2 MΩ cm) was used in this work, and all chemicals used were of analytical grade.

2.2 Preparation of GA-metal ion hydrogels (GA-M^{n+})

A stock solution of GA (4 wt%) was prepared by dissolving GA powder in water and heating it at 80 °C under mild agitation to obtain a transparent solution. Various salt solutions (NaCl, KCl, $CaCl_2$, $ZnCl_2$, $AlCl_3$, and $FeCl_3$, 1 M) were prepared by dissolving salts in water and adjusting the pH to 4.0 to prevent hydrolysis. Then, GA solution and salt solutions were completely mixed at different volume ratios under the heating condition (80 °C) to acquire the desired sample concentration. The resultant samples were stored overnight (12 h) at room temperature (25 °C) before further use. The corresponding hydrogels are termed GA-Na^+, GA-K^+, GA-Ca^{2+}, GA-Zn^{2+}, GA-Al^{3+}, and GA-Fe^{3+}, respectively. The gelation of sample was determined by the tube inverted test, and the gel formation was verified if no visual fluidity was observed after 1 min of tube inversion.

2.3 Rheological measurements

The rheological properties of GA and GA-M^{n+} hydrogels were investigated using a Haake MARS60 rheometer (Haake, Germany), and a parallel plate geometry (35 mm diameter, 1 mm gap) was used. All measurements were carried out at 25 °C and samples were allowed to relax for 2 min before rheological tests.

2.3.1 SAOS measurements

The SAOS measurements were conducted with frequency sweeps. Frequency sweep tests were performed with the angular frequency range from 0.1 to 100 rad/s, while the strain was kept constant at 0.1% in the linear viscoelastic region (LVR). The damping factors (G″/G′) were collected from the frequency sweeps. The power-law model, $G' = K{\cdot}\omega^m$, was further fitted on the frequency sweep results, and the corresponding exponent, m, was calculated. The coefficient K is the power-law constant (Pa s^n), and m is the frequency exponent (dimensionless).

2.3.2 LAOS measurements

LAOS measurements were performed with strain sweep tests, which were measured over the strain range of 0.01–1000% at a fixed angular frequency of 6.28 rad/s. The yield strain is defined here as the value of the strain amplitude at which the storage modulus (G′) deviates by more than 5% from its strain-independent value within the LVR [44,45], and correspondingly, the yield stress is the stress observed at the yield strain. Additionally, the flow strain and stress are defined as the strain and stress values at the crossover point, where the G′ equals the loss modulus, G″ [46]. Based on these definitions, the rheological behaviors of hydrogels can be quantified and accurately characterized.

To analyze the nonlinear responses of hydrogels, the torque-deformation waveform data was collected at different strains (1, 5, 11, 49, 98, and 500%) with a constant angular frequency (6.28 rad/s). According to the method of McKinley and co-workers [47], based on a Chebyshev polynomial based stress decomposition, the torque-deformation waveform data can be further analyzed using the MITLaos software (Version 2.2 beta), to construct Lissajous-Bowditch plots and determine the Chebyshev coefficients. The intracycle strain stiffening ratio (S factor) and intracycle shear thickening ratio (T factor), as defined in Eqs (1) and (2), were determined.

$$S = \frac{G'_L - G'_M}{G'_L} \tag{1}$$

$$T = \frac{\eta'_L - \eta'_M}{\eta'_L} \tag{2}$$

In Eq. (1), G'_L is the large-strain modulus or secant modulus evaluated at the maximum imposed strain, and G'_M is the minimum-strain modulus or tangent modulus at γ=0. In Eq. (2), η'_L is the large-rate dynamic viscosity, and η'_M is the minimum-rate dynamic viscosity [47].

The dissipated energy (E_d) and phase angle (δ) were collected from the normalized elastic Lissajous curves. The dissipated energy per unit volume, $E_d = \oint \tau d\gamma$, is determined by the area enclosed by the Lissajous curves in the elastic projection during a single LAOS cycle [48]. The phase angle (δ) represents the angular difference between the material response and the applied deformation and serves as a measure of the material elasticity or viscosity [23].

2.4 Cryo scanning electron microscopy (Cryo-SEM)

The GA and GA-M^{n+} hydrogel samples were fixed on a holder and snap-frozen with liquid nitrogen slush before being transferred into a cryo chamber (PP3010T, Quorom, UK) at −140 °C. The samples were afterward sublimated for 30 min at −90 °C to remove frost artifacts. Finally, the samples were scanned with a scanning electron microscope (S-4800, Hitachi) at 3 kV.

2.5 Field emission scanning electron microscopy (FE-SEM)

The microstructures of freeze-dried GA and GA-M^{n+} samples were observed on a Zeiss Merlin field emission scanning electron microscope (Zeiss, Germany). The samples were carefully transferred and firmly attached to a holder, and then sputter-coated with gold (JEOL JFC-1200 fine coater, Japan) before imaging at 5 kV.

2.6 Transmission electron microscopy (TEM)

A droplet of GA and GA-M^{n+} solutions was dropped onto a carbon-coated copper grid, and the excess sample was removed with

filter paper after 30 s. Then, samples were negatively stained by a droplet of 2% uranyl acetate for 30 s. The morphology was observed on a JEM-1400 Plus transmission electron microscope at 120 kV (JEOL, Japan).

2.7 Fourier transform infrared spectroscopy (FTIR)

The FTIR spectra of freeze-dried GA and GA-M^{n+} hydrogels were recorded at 4000−400 cm^{-1} using an FTIR spectrophotometer (Bruker, Germany) equipped with a narrow-band mercury cadmium telluride detector with a resolution of 2 cm^{-1}.

2.8 X-ray photoelectron spectroscopy (XPS)

XPS measurements were performed using a Kratos Axis Supra$^+$ XPS instrument (Kratos, UK). Al Kα radiation was used, and the chamber pressure was less than 5×10^{-9} torr during operation. The XPS spectra were scanned with the pass energy of 160 eV and 40 eV for full and narrow spectra, respectively. Thermo Scientific Avantage software was used for data analysis. The data was calibrated based on the C 1 s peak at 284.8 eV, and a smart-type background was used.

2.9 Density functional theory (DFT) calculation

The structures and binding energies formed by GA with metal ions (Na^+, K^+, Ca^{2+}, Zn^{2+}, Al^{3+}, and Fe^{3+}) were calculated based on density functional theory. All calculations were performed using the ORCA (version 5.0.3) program [49–52] at the B3LYP-D3 and def2-SVP basis set levels for conformational optimization and vibrational analysis, and single point energy calculations were performed at the def2-TZVP level using the more accurate wB97M-V function [53]. The Conductor-like Continuum Polarization Model CPCM Solvation models (SMD) were implemented for water solvation. Data analysis was carried out using VESTA software [54]. Taking single-charged cations as an example, the binding energies (E_b) were calculated based on the following equation:

$$RCOO^- + X^+ \rightarrow RCOOX \quad (3)$$

where $RCOO^-$ and X^+ denote deprotonated carboxylic acid and cation, respectively. E_b is defined as $E_b = E_{RCOOX} - E_{RCOO^-} - E_{X^+}$ (we will display and discuss absolute values for convenience).

2.10 Zeta potential measurements

The zeta potentials of GA and GA-M^{n+} samples were measured using a Zetasizer Nano ZS (Malvern, UK). The measurements were carried out at 25 °C in triplicate.

2.11 Statistical analysis

All testing was performed in triplicate unless specifically mentioned and results were presented as mean ± standard deviation for all measurements. One-way Analysis of variance (ANOVA) of the data was performed using the OriginPro 2021 software. LSD's test was used for the comparison of mean values among samples using a level of significance of 5%.

3 Results and discussion

3.1 Gelation experiments

The influence of metal ions with varying valence states on the gelation behavior of GA was first investigated, when the concentration of GA exceeds or falls below the critical gelation concentration (CGC, 0.3 wt%) [17]. As illustrated in Fig. S1, for the GA concentration (0.25 wt%) below CGC, both monovalent metal ions (Na^+ and K^+) at 1–100 mM and divalent metal ions (Ca^{2+} and Zn^{2+}) at 1–5 mM facilitated the gelation process, leading to the gel formation below CGC. Al^{3+} also promoted gelation at a concentration of 1 mM, while Fe^{3+} did not exhibit such promoting effects. When the GA concentrations (1 and 2 wt%) exceed CGC, the gel formation and appearance were not affected visually by the monovalent metal ions (Na^+ and K^+), yet the polyvalent metal ions exhibited a significantly different influence on the gelation behavior of GA, which appears that the higher ion concentrations can hinder the gelation of GA. As can be seen, for the system of 1 wt% GA, the gels cannot be formed in the presence of divalent metal ions (Ca^{2+} and Zn^{2+}) at 25 mM or more, especially for the GA-Ca^{2+}, and the systems became cloudy and opaque. This is more evident for the GA systems with the trivalent metal ions (Al^{3+} and Fe^{3+}), where the gel formation was more obviously inhibited, even at a low ion concentration of 2.5 mM (i.e., Fe^{3+}). These gelation tests point out the specific ion effects on the formation and properties of GA supramolecular hydrogels.

To gain the insight into the complexation between GA and metal ions, we selected the GA with a concentration of 2 wt% as a model system for the subsequent experiments, in order to more directly show the impact of metal ions on the rheological behavior and microstructure of GA hydrogels. In addition, the 5 mM and 50 mM were chosen as representative low and high concentrations of various metal ions to investigate the properties of GA-M^{n+}, and their corresponding hydrogels are termed as GA-5M^{n+} and GA-50M^{n+}, respectively. Since the GA formed a precipitate with the addition of 50 mM Fe^{3+}, the subsequent characterization of this system was excluded.

3.2 Linear rheological properties

Frequency sweeps (0.1–100 rad/s) of GA-M^{n+} were determined at a small strain (0.1%, within the LVR). As can be seen from Fig. 1a,b, the storage modulus (G′) for each case was consistently higher than the loss modulus (G″), pointing to the mostly elastic solid-like behavior of these hydrogels. In the presence of low ion concentration of 5 mM, the GA-5Na^+, GA-5K^+, and GA-5Fe^{3+} showed similar rheological responses to pure GA hydrogel (0 mM). However, the GA-5Ca^{2+}, GA-5Zn^{2+}, and GA-5Al^{3+} exhibited significantly higher G′ and G″, indicating the greater viscoelasticity (Fig. 1a). For all GA-M^{n+} samples with high ion concentration of 50 mM, both G′ and G″ were larger than those of pure GA hydrogel (Fig. 1b). Moreover, it can be clearly seen that GA-50Na^+ and GA-50K^+ showed significantly higher values of G′ and G″ than these hydrogels with polyvalent metal ions (GA-50Ca^{2+}, GA-50Zn^{2+}, and GA-50Al^{3+}). The damping factor (G″/G′) serves as an indicator of the relative contribution of the viscous and elastic components to the viscoelastic response of hydrogels. Fig. 1c,d shows the damping factors (G″/G′) of these hydrogels at a constant frequency of 6.28 rad/s. As presented in Fig. 1c, at low ion concentration of 5 mM, compared to pure GA and the GA-5Na^+ and GA-5K^+, which had similar damping factor values, the GA-5Ca^{2+}, GA-5Zn^{2+}, and GA-5Al^{3+} (and even GA-5Fe^{3+}) showed significantly lower values of damping factor, indicating a relatively

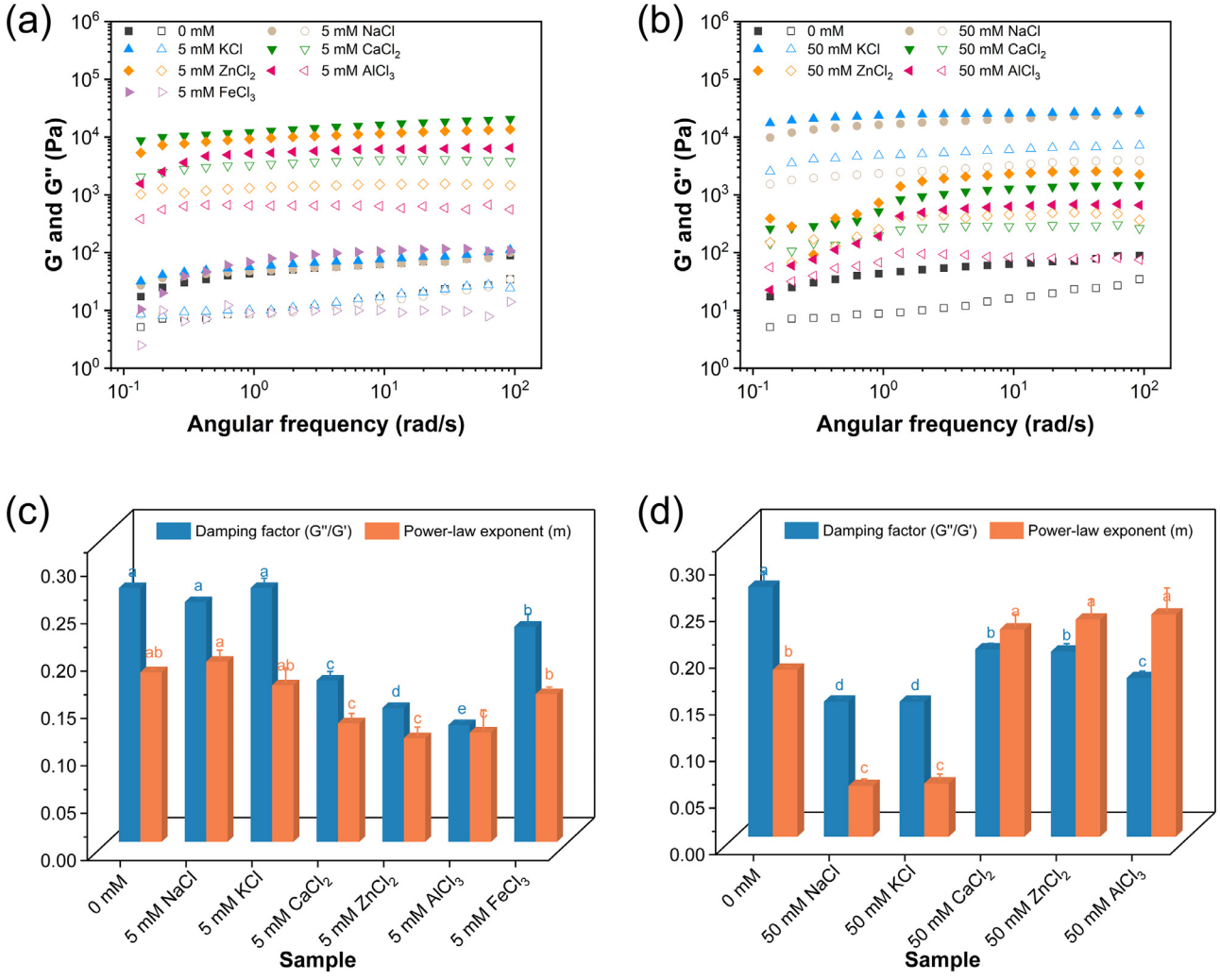

Fig. 1

Frequency sweeps of 2 wt% GA with various metal ions at 5 mM (a) and 50 mM (b). G′ and G″ are shown as filled and open symbols, respectively. Damping factor and power-law exponent of 2 wt% GA with various metal ions at 5 mM (c) and 50 mM (d).

more elastic response. In contrast, at high ion concentration of 50 mM, an opposite trend was observed for these GA-M^{n+}, where the damping factor values of the GA-50Na^+ and GA-50K^+ were significantly lower than the GA-50Ca^{2+}, GA-50Zn^{2+}, and GA-50Al^{3+} samples (Fig. 1d). Further, power-law model equations of G′ against frequency were used to describe the frequency dependence of the GA-M^{n+}hydrogels (Fig. 1c,d). For an ideal solution, the power-law exponent m is equal to 1, while $m = 0$ corresponds to a perfect gel [55]. At a metal ion concentration of 5 mM, the GA-5Na^+ and GA-5K^+ displayed similar exponent m values to the pure GA, which were significantly higher than the GA-5Ca^{2+}, GA-5Zn^{2+}, and GA-5Al^{3+} (Fig. 1c). Conversely, at a high metal ion concentration (50 mM), both GA-50Na^+ and GA-50K^+ showed significantly lower m values (around 0.05) than pure GA (around 0.18) and the GA-50Ca^{2+}, GA-50Zn^{2+}, and GA-50Al^{3+}, and the m values of the latter three GA-50M^{n+}samples were very high (around 0.23, Fig. 1d), pointing to an unstable gel structure. The results (Fig. 1c,d) of damping factor and power-law exponent are in good agreement with the frequency sweep results (Fig. 1a,b), which implies that the specific type and concentration effects of metal ions on the linear rheological properties of GA supramolecular hydrogels, and the influence of polyvalent metal ions appears to be more pronounced than the monovalent metal ions.

3.3 Nonlinear rheological properties

3.3.1 Response to large strain deformations

To obtain more insights into the viscoelastic behavior and establish the relationship between the rheological properties and structural changes under large deformations, large amplitude oscillatory shear (LAOS) experiments were further carried out [56]. Strain sweep results of the GA-M^{n+} were presented in Fig. 2a,b. For all the investigated cases, the values of G′ were higher than G″ within the LVR, and the effects of the type and concentration of these metal ions on the linear rheological properties of GA supramolecular hydrogels were similar to those observed from the results of frequency sweeps (Fig. 1a,b), which further confirms that the rheological properties of GA hydrogels can be highly adjusted by metal ion complexation. The texture maps based on the stress and strain values at the end of the LVR and at the crossover

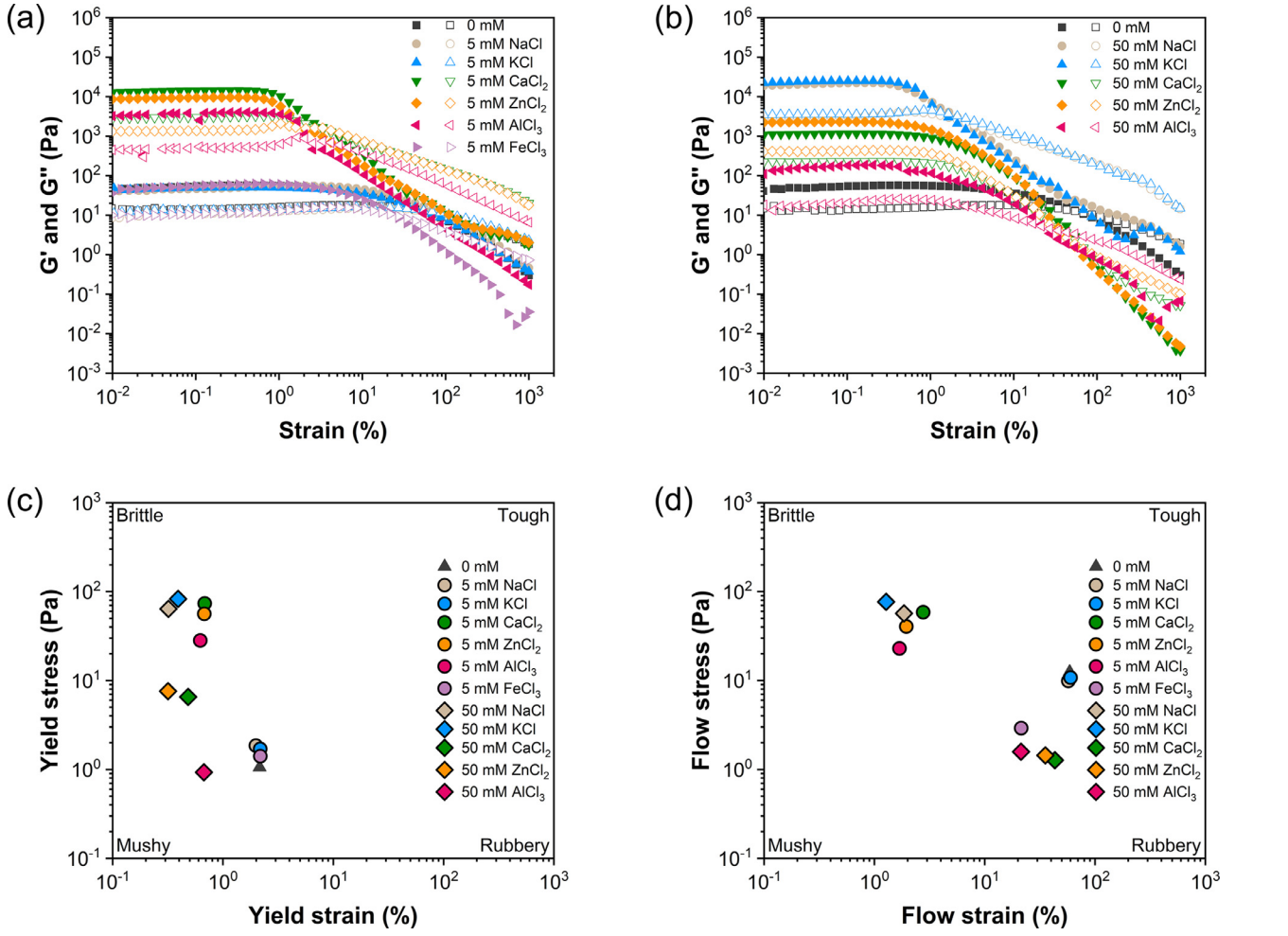

Fig. 2

Strain sweeps of 2 wt% GA with various metal ions at 5 mM (a) and 50 mM (b). G′ and G″ are shown as filled and open symbols, respectively. Texture maps at the end of the LVR (c) and at the crossover point (d) for 2 wt% GA with various metal ions.

point were depicted in Fig. 2c,d, respectively. The yield strain is defined here as the value of the strain amplitude at which the G′ deviates by more than 5% from its strain-independent value within the LVR [44,45], and correspondingly, the yield stress is the stress observed at the yield strain. The flow strain and stress are defined as the strain and stress values at the crossover point, where the values of G′ and G″ are equal [46]. As can be observed, the rheological properties of all samples largely depended on the shear stress and shear strain applied. In general, for samples with low shear stress and shear strain, such as grits, a mushy consistency is observed. On the other hand, samples with low shear stress and high shear strain, like gelatin, exhibit a rubbery texture. In the case of high shear stress and shear strain, as seen in fruit leather, the sample tends to be tough, whereas the samples with high shear stress and low shear strain, such as baked or confectionery food products, display a brittle nature [57]. As seen in Fig. 2c, at a metal ion concentration of 5 mM, the GA-5Na^+, GA-5K^+, GA-5Fe^{3+}, and pure GA samples possessed relatively low yield strain and yield stress, indicating a mainly mushy behavior, yet the GA-5Ca^{2+}, GA-5Zn^{2+}, and GA-5Al^{3+} were relatively more brittle. When the metal ion concentration was increased to 50 mM, the GA-50Na^+ and GA-50K^+ obviously shifted the texture from mushy to brittle, whereas the GA-50Ca^{2+}, GA-50Zn^{2+}, and GA-50Al^{3+} became mushier. We then assessed the texture map at the crossover point (Fig. 2d), which is more sensitive to structural discrepancies compared to that at the end of the LVR (Fig. 2c). In comparison with the GA-5Na^+, GA-5K^+, and pure GA, which showed similar texture properties in hardness and deformability at the crossover point, the GA-5Ca^{2+}, GA-5Zn^{2+}, and GA-5Al^{3+} materials became brittle. At 50 mM metal ion concentration, the GA-50Na^+ and GA-50K^+ were commonly brittle, whereas the GA-50Ca^{2+}, GA-50Zn^{2+}, and GA-50Al^{3+} were characterized as mushy and became softer with reduced crossover stress. This means that compared to the monovalent metal ions, the polyvalent metal ions at higher concentrations (e.g., 50 mM) exert a detrimental effect on the texture properties of GA supramolecular hydrogels, resulting in significantly lower flow stress and moduli beyond the LVR.

3.3.2 Analysis of Lissajous-Bowditch curves

Elastic and viscous Lissajous-Bowditch curves, which display the instantaneous intracycle stress of the materials as a function

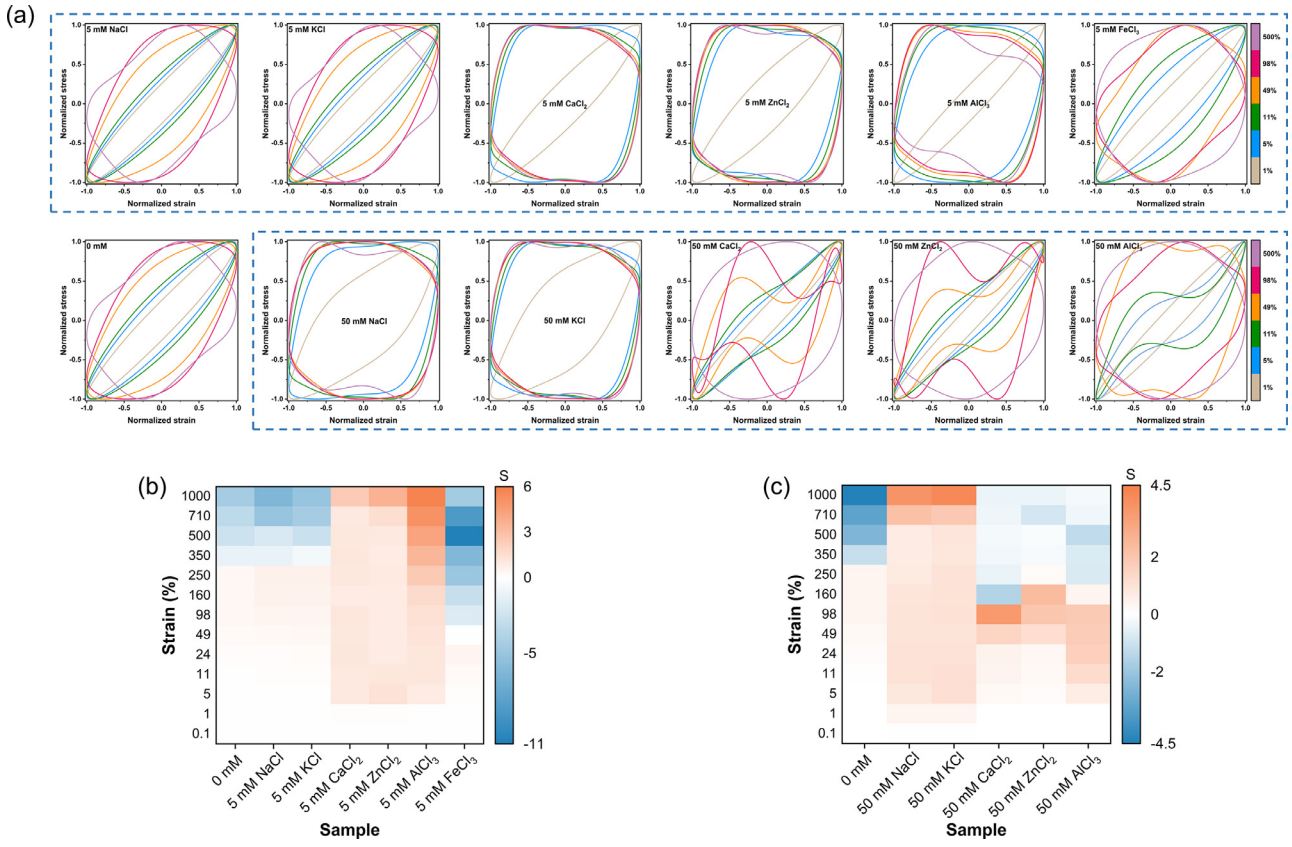

Fig. 3

(a) Elastic Lissajous-Bowditch loops of 2 wt% GA with various metal ions at 5 mM and 50 mM, acquired at the frequency of 6.28 rad/s and different strains of 1, 5, 11, 49, 98, and 500%. Stress and strain data are normalized with respect to their corresponding maximum values in the oscillation cycle. Strain stiffening ratio (S factor) of 2 wt% GA with various metal ions at 5 mM (b) and 50 mM (c).

of the applied strain or shear rate, can not only facilitate the qualitative assessment of nonlinear viscoelastic properties but also provide helpful information about intracycle nonlinear responses [47]. Typically, for a perfectly elastic material, the elastic projection of the Lissajous-Bowditch loops in the LVR appears as a straight line, and for a purely viscous material, it exists in the form of a circle. Since both the stress and strain waveforms are sinusoidal and only contain the first harmonic coefficient, the response of a viscoelastic material in the LVR results in an elliptical shape of the Lissajous-Bowditch curve. Any deviation from the elliptical shape of Lissajous-Bowditch curves indicates that the LVR has been exceeded and that higher harmonics have emerged in the stress and strain waveforms, which lead to distortions in the sinusoidal signal responses [48,56].

The elastic Lissajous-Bowditch loops of the GA-M^{n+} were presented in Fig. 3a at different strain amplitudes (1, 5, 11, 49, 98, and 500%). All stress and strain data were normalized with respect to their corresponding maximum values in the oscillation cycle. The elastic Lissajous curves of the GA-$5Na^{+}$ and GA-$5K^{+}$ exhibited a narrow elliptical shape under low strain amplitudes (1–11%), indicating a linear viscoelastic solidlike behavior (predominantly elastic), which is in accordance with the pure GA sample. As the strain amplitude increased, the Lissajous curves exhibited expanded ellipses (11–49% strain amplitudes) and were transformed into nearly quadrilateral patterns (98–500% strain amplitudes), signifying an escalation in viscous dissipation during intracycle deformation and a transition from a state dominated by elasticity to one dominated by viscosity. These specific shape distortions of the elastic Lissajous curves occurred more promptly and vigorously in GA-$5Ca^{2+}$, GA-$5Zn^{2+}$, GA-$5Al^{3+}$, and GA-$5Fe^{3+}$, notably in GA-$5Ca^{2+}$, GA-$5Zn^{2+}$ and GA-$5Al^{3+}$, where the curves turned from elliptical to quadrilateral even at 5% strain amplitude. At 50 mM metal ion concentration, the GA-$50Na^{+}$ and GA-$50K^{+}$ expressed a more intense distortion with the elastic Lissajous curves at 1% strain being nearly quadrilateral and the area encompassed by the curves growing wider. Interestingly, the elastic Lissajous curves of the GA-$50Ca^{2+}$ and GA-$50Zn^{2+}$ changed from ellipse to a bow-tie shape at 49–98% strain amplitudes, which also can be observed in GA-$50Al^{3+}$ at 5–11% strain amplitudes. This specific shape of the Lissajous-Bowditch curves indicates an overshoot in the stress, which is mainly attributed to the coupling between the material elasticity and the effects of instrument inertia [58]. The observed nonlinear response with increasing strain amplitudes can be attributed to the microstructural changes occurring within the GA supramolecular hydrogels during intracycle deformations. These changes involved elastic straining, occurring at strain amplitudes of 1–11% for pure GA, GA-$5Na^{+}$, and GA-$5K^{+}$ (with lower strain

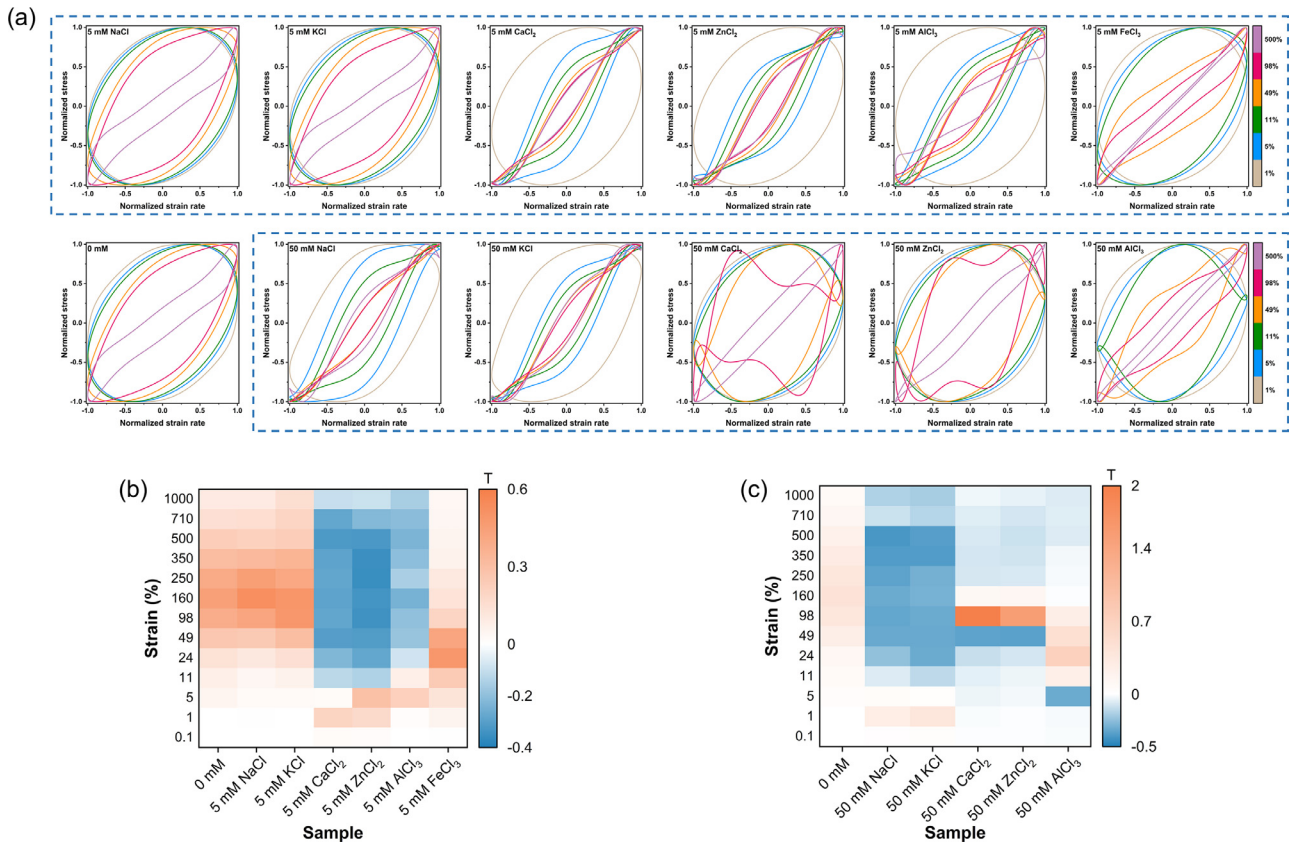

Fig. 4

(a) Viscous Lissajous-Bowditch loops of 2 wt% GA with various metal ions at 5 mM and 50 mM, acquired at the frequency of 6.28 rad/s and different strains of 1, 5, 11, 49, 98, and 500%. Stress and strain rate data are normalized with respect to their corresponding maximum values in the oscillation cycle. Shear thickening ratio (T factor) of 2 wt% GA with various metal ions at 5 mM (b) and 50 mM (c).

amplitudes observed for GA-50Ca^{2+}, GA-50Zn^{2+}, and GA-50Al^{3+}). Subsequently, at higher strains, the supramolecular hydrogels exhibited yielding, flow, and subsequent recovery of the gel structure. Fig. 3b,c provides more detailed insights into the elastic nonlinear behavior through the analysis of the strain stiffening ratio S. The S factors of the GA-5Na^{+} and GA-5K^{+} (and also GA-5Fe^{3+}) were close to 0 at 1–5% strain amplitudes, resembling that of pure GA, which suggests a linear elastic response, and then the values of S factors switched from positive (>0, intracycle strain stiffening) to negative (<0, intracycle strain softening) as the strain amplitude went up (Fig. 3b). In contrast, the S factors of GA-5Ca^{2+}, GA-5Zn^{2+}, GA-5Al^{3+}, GA-50Na^{+}, and GA-50K^{+} approached approximately 1 even at 5% strain amplitude, displaying the nonlinear behavior, and were positive over the entire strain amplitudes (0.1–1000%), showing the intracycle strain stiffening. Note that this intracycle stiffening should not be confused with the overall response of these materials, which exhibited strain softening [59], as illustrated in Fig. 2a,b. In addition, the S factors of GA-50Ca^{2+}, GA-50Zn^{2+}, and GA-50Al^{3+} shifted from positive to negative at 160–250% strain amplitudes and subsequently tended to manifest a weak intracycle strain softening.

Fig. 4a shows the viscous Lissajous-Bowditch loops of GA-M^{n+} at different strain amplitudes (1, 5, 11, 49, 98, and 500%). All stress and strain rate data were normalized with respect to their corresponding maximum values in the oscillation cycle. As can be seen, the viscous Lissajous curves of GA-5Na^{+} and GA-5K^{+} exhibited a perfect elliptical shape under low strain amplitudes (1–11%), indicating a linear viscoelastic solidlike behavior, followed by a change to the sigmoidal curve at 49–500% strain amplitudes. These shape changes of Lissajous curves are in good agreement with those in pure GA sample. Conversely, the distinct shape distortions of the viscous Lissajous curves occurred more rapidly and violently in GA-5Ca^{2+}, GA-5Zn^{2+}, GA-5Al^{3+}, GA-50Na^{+}, and GA-50K^{+}, and it is noteworthy that at strain amplitudes of 11–500%, the secondary loops appeared in the curves, suggesting the presence of significant nonlinearity in the elastic stress responses. The appearance of the secondary loops is typically associated with the microstructure rearrangements occurring at a shorter timescale compared to the timescale of deformation [60]. The viscous Lissajous curves of GA-50Ca^{2+}, GA-50Zn^{2+}, and GA-50Al^{3+} shifted from elliptical to sigmoidal at strain amplitudes of 11–49%. More detailed insights into the viscous nonlinear behavior can be further obtained from the shear thickening ratio T (Fig. 4b,c). As can be seen, the T factors were positive for pure GA, GA-5Na^{+}, and GA-5K^{+} (and also GA-5Fe^{3+}) in the whole range of strain amplitude (0.1–1000%) indicating the intracycle shear thickening. Similarly, this intracycle shear thickening should not

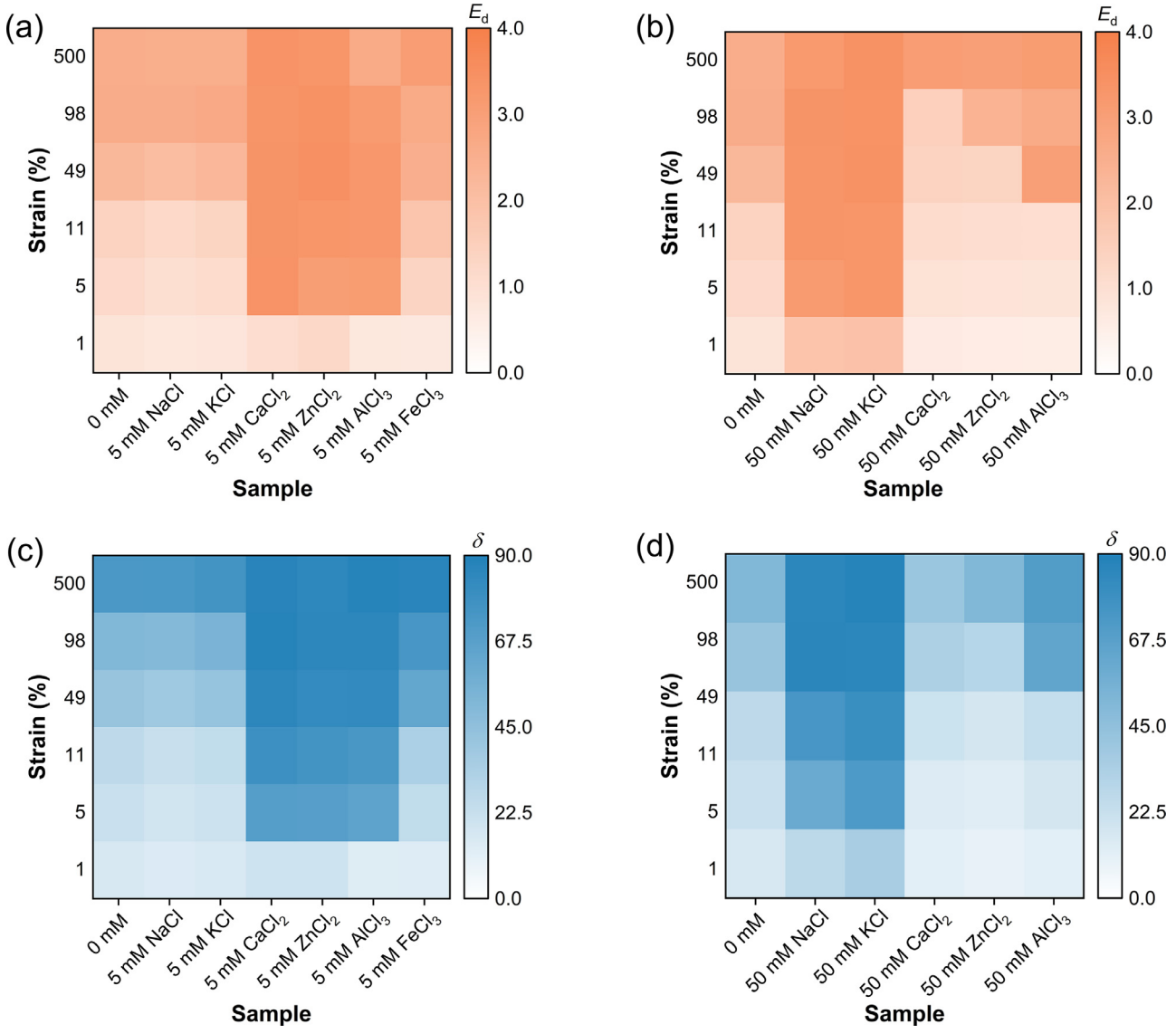

Fig. 5

Dissipated energy (a and b) and phase angle (c and d) of 2 wt% GA with various metal ions at 5 mM (a and c) and 50 mM (b and d) under large amplitude oscillatory shear.

also be confused with the overall response of these hydrogels, which were characterized as shear thinning, as illustrated in Fig. 2a,b. As a contrast, the T factors of GA-5Ca^{2+}, GA-5Zn^{2+}, GA-5Al^{3+}, GA-50Na^{+}, and GA-50K^{+} were positive at low strain amplitudes (0.1–5%) but became negative as the strain amplitudes rose to 11–1000%, showing an intracycle shear thinning, which implied that the gel networks were broken and became a more fluid-like behavior under the influence of intense shear fields at higher strains. The T factors of GA-50Ca^{2+}, GA-50Zn^{2+}, and GA-50Al^{3+} experienced a multiple change from negative to positive and then to negative, which may be related to the instability of their gel structure (Fig. 1b).

The dissipated energy (E_d) and phase angle (δ), derived from the normalized elastic Lissajous curves, serve as valuable parameters to assess the nonlinear response of the materials (Fig. 5). The dissipated energy per unit volume, $E_d = \oint \tau d\gamma$, is determined by the area enclosed by the Lissajous curves in the elastic projection during a single LAOS cycle [48]. In the case of a perfectly plastic material, the dissipated energy is defined as $E_d = (2\gamma_{max}) \cdot (2\tau_{max})$, resulting in a value of 4 for the normalized Lissajous curves [61]. Conversely, a purely elastic material has an E_d value of 0. Therefore, in the normalized Lissajous curves, values of $0 < E_d < 4$ indicate a viscoelastic behavior. The phase angle (δ) represents the angular difference between the material response and the applied deformation and serves as a measure of the material elasticity or viscosity [23]. A perfectly elastic material has a phase angle of $\delta = 0°$, while a purely viscous material has a phase angle of $\delta = 90°$ For all the investigated cases, both E_d and δ exhibited a significant increase with increasing strain amplitude, demonstrating a transition from the elastic-dominated to the viscous-dominated behavior in the LAOS responses (Fig. 5), which can be ascribed to the dissociation of interfibrillar interactions and

bonds thus leading to the structural degradation of gel network under large shear deformations [62]. The pure GA, GA-5Na^+, and GA-5K^+ showed overall similar values of dissipated energy and phase angle as a function of strain amplitude (Fig. 5a,c), in good agreement with the results of elastic and viscous Lissajous-Bowditch curves (Figs. 3 and 4). Compared to pure GA, the values of dissipated energy and phase angle for GA-5Ca^{2+}, GA-5Zn^{2+}, GA-5Al^{3+}, GA-50Na^+, and GA-50K^+ increased more drastically and exhibited a sharp jump at 5% strain amplitude, which suggests that the fibrillar network of the supramolecular hydrogels, as the main source of viscous dissipation, may be largely dissociated, as observed in the corresponding Lissajous curves (Figs. 3a and 4a).

On the basis of the aforementioned results (Figs. 2-5), it can be concluded that the nonlinear rheological properties of GA supramolecular hydrogels were also strongly affected by the type and concentration of metal ions. The GA-5Na^+ and GA-5K^+ possessed similar nonlinear rheological responses to pure GA, which showed the transition from intracycle strain stiffening to intracycle strain softening at high strain amplitudes, suggesting that the gel networks became loose during large deformations, as well as the intracycle shear thickening behavior due to the reformation of physical interactions. In contrast, the GA-5Ca^{2+}, GA-5Zn^{2+}, GA-5Al^{3+}, GA-50Na^+, and GA-50K^+ demonstrated a pronounced nonlinear rheological behavior with a faster transition from elastic to viscous dominance, where the intracycle strain stiffening behavior can be mainly attributed to the increased contact of the GA fibrils, requiring higher shear stress for further deformation and consequently leading to a stiffer network. Additionally, the intracycle shear thinning behavior arises from insufficient relaxation time at high strain amplitudes, resulting in a delayed reformation of physical interactions. The Lissajous curves of GA-50Ca^{2+}, GA-50Zn^{2+}, and GA-50Al^{3+} exhibited erratic shapes with increasing strain amplitudes, accompanied by fluctuating T factors shifting between positive and negative values, which is ascribed to the inherent instability of the gel network, rendering them vulnerable to external deformations and perturbations. Taken together, these results indicate that compared to the monovalent metal ions, the incorporation of the polyvalent metal ions especially at high concentrations (e.g., 50 mM) may tend to disrupt the fibrillar network structure of GA gels, leading to the irregular nonlinear rheological responses and the lower resistance to large deformations.

3.4 Morphology and structural properties

To further clarify the impact of metal ions on the structural characteristics of GA supramolecular hydrogels and to establish a correlation between their rheological behaviors and microstructure, the microstructure of these GA-M^{n+} hydrogels was visualized by using a variety of microscopy techniques. The effect of the presence of various metal ions on the properties of self-assembled GA nanofibrils was first investigated. As seen from the TEM images (Fig. S2), the incorporation of Na^+ and K^+ with 5 and 50 mM, as well as Ca^{2+} and Zn^{2+} with 5 mM did not substantially affect the microstructure of GA nanofibrils; however, an obvious fibril association was observed in GA-5Ca^{2+}, GA-5Zn^{2+}, GA-50Na^+ and GA-50K^+, which is attributed to the reduced electrostatic repulsion between GA nanofibrils and thereby the increased interfibrillar binding [63]. In addition, it is noted that the fibrillar structure within the systems of GA-5Al^{3+}, GA-50Ca^{2+}, GA-50Zn^{2+} and GA-50Al^{3+} appeared to be disrupted leading to the formation of shorter fibrillar aggregates.

For the microstructure observation of GA-M^{n+} hydrogels, the FE-SEM images (Fig. S3) manifested that all samples exhibited a relatively uniform and interconnected 3D porous network structure, apart from the GA-50Ca^{2+}, GA-50Zn^{2+}, and GA-50Al^{3+}. The network structure of GA-50Ca^{2+} and GA-50Zn^{2+} appeared to be broke down and presents an aggregated state with the formation of large aggregates and clusters, especially in the GA-50Al^{3+}, which can be explained by the structural dissociation of GA nanofibrils in the presence of high concentration (50 mM) of polyvalent metal ions (Fig. S2). Cryo-SEM measurements were further carried out to observe the pristine structure of the wet hydrogel samples, and the results were illustrated in Fig. 6. As can be seen, pure GA and GA-5K^+ showed similar pore size (around 2.9–3.5 μm in diameter). In contrast, the pore size of GA-5Zn^{2+} and GA-50K^+ increased obviously with an increase in the pore wall thickness (Fig. S5), especially for the GA-50K^+, which displayed a relatively more compact and ordered fibrous network (Fig. 6d). Additionally, it seems that the pore microstructures of the GA-M^{n+} with polyvalent metal ions were mainly transformed into irregular shapes, and as can be observed, the GA-50Zn^{2+} aggregated to large, unshaped, discrete clusters, which is in line with the FE-SEM results (Fig. S3). Energy-dispersive X-ray spectroscopy (EDS) further confirmed that for the more ordered network structures (e.g., GA-50K^+, Fig. 6f), the metal ions appeared to be more evenly distributed within the matrix and partially free in the pores (Fig. 6i), whereas for aggregated irregular structures (e.g., GA-50Al^{3+}, Fig. 6g), the metal ions were mainly concentrated within the aggregates and clusters (Fig. 6h). This suggests that the metal ions with different valences exhibited different distribution patterns depending on the type of network structure formed in the GA-M^{n+} system. Taken together, these results suggest that compared to pure GA, GA-5Na^+ and GA-5K^+, which showed similar microstructures, the GA-5Ca^{2+}, GA-5Zn^{2+}, GA-5Al^{3+}, GA-50Na^+, and GA-50K^+ possessed a relatively more compact and ordered gel network due to the reduced electrostatic repulsion and thereby the increased binding between GA fibrils. By comparison, owing to the structural dissociation of GA nanofibrils, the GA-50Ca^{2+}, GA-50Zn^{2+} and GA-50Al^{3+} (especially the GA-50Al^{3+}) formed irregular and discrete aggregated network structures. These observations indicate that the type and concentration of metal ions can significantly impact the microstructure of GA supramolecular hydrogels, which well explains their linear and nonlinear rheological behaviors and particularly the resistance to large deformations.

FTIR were then performed to characterize the interaction between GA and metal ions. As shown in Fig. 7b, pure GA possessed main characteristic peaks at around 3600–3200, 2945/2872, 1726, 1657, 1398, 1215, 1172, and 1041 cm^{-1}, ascribed to O–H stretching vibration, C–H stretching vibration of $–CH_3$ groups, C = O stretching vibration, C = C stretching vibration in triterpene skeleton, C–H bending vibration of $–CH_3$ groups, C–O stretching vibration, C–O–C stretching vibration

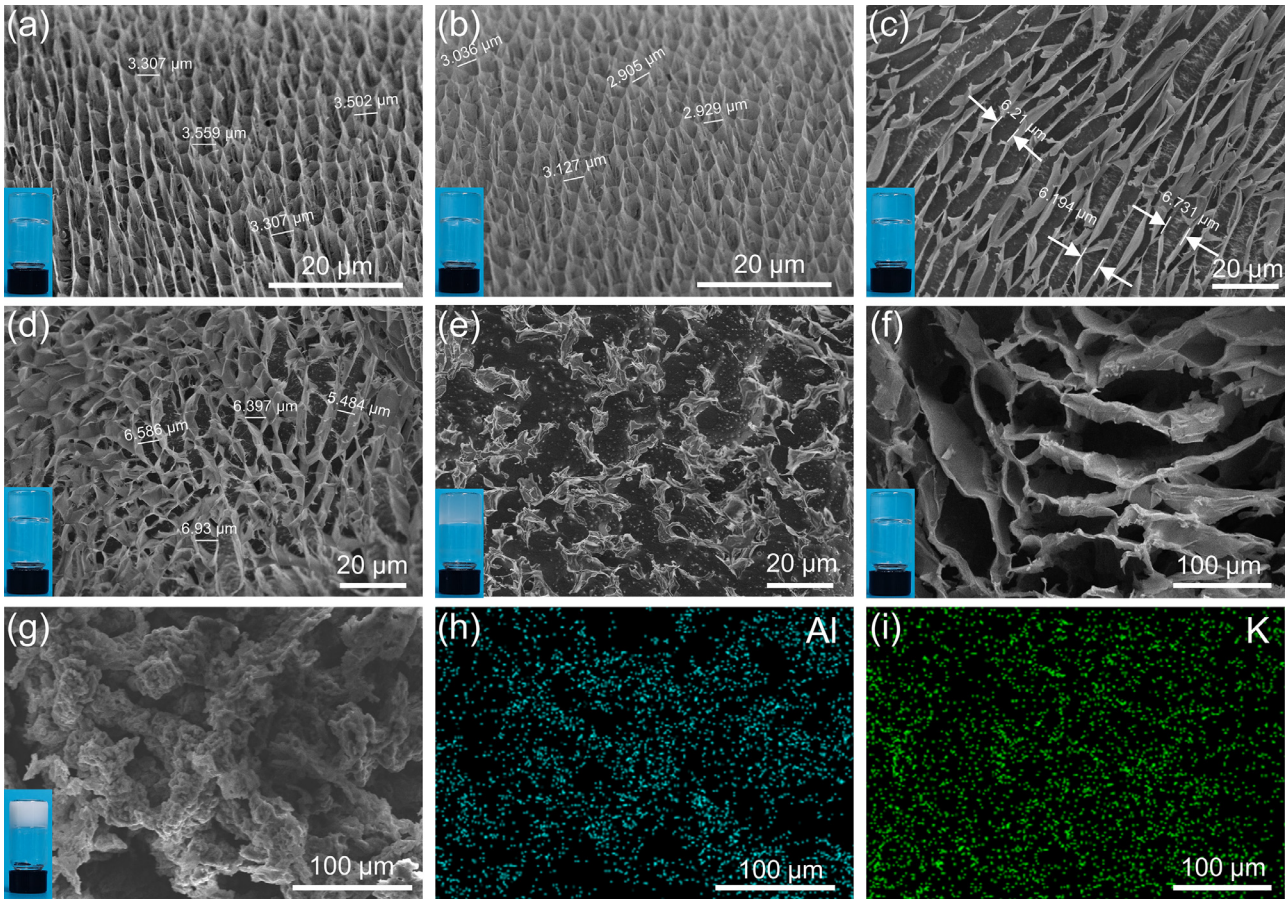

Fig. 6

(a-e) Cryo-SEM images of 2 wt% GA with various metal ions: (a) 0 mM, (b) 5 mM KCl, (c) 5 mM $ZnCl_2$, (d) 50 mM KCl, and (e) 50 mM $ZnCl_2$. (f and i) FE-SEM image and EDS mapping (K element) of GA-50K^+. (g and h) FE-SEM image and EDS mapping (Al element) of GA-50Al^{3+}.

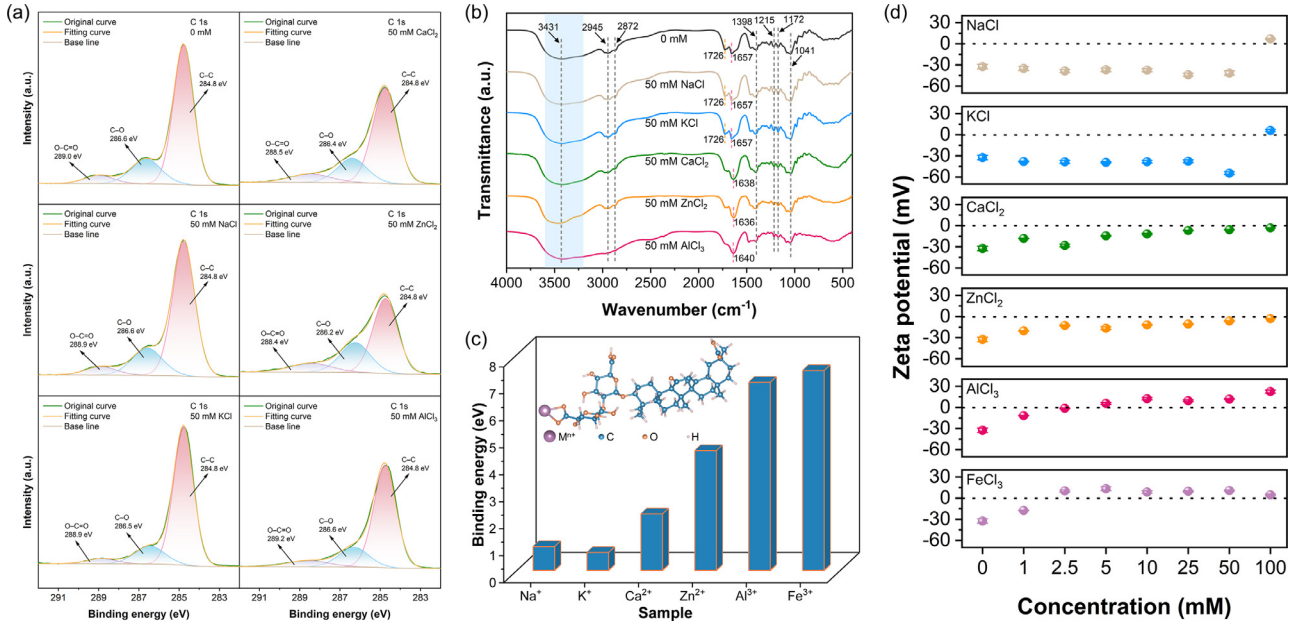

Fig. 7

High-resolution XPS C 1 s spectra (a) and FTIR spectra (b) of 2 wt% GA with various metal ions at 50 mM. (c) The binding energy of GA-metal ions complex by DFT calculations (absolute values for convenience were used). (d) Zeta potential of 0.1 wt% GA with various metal ions.

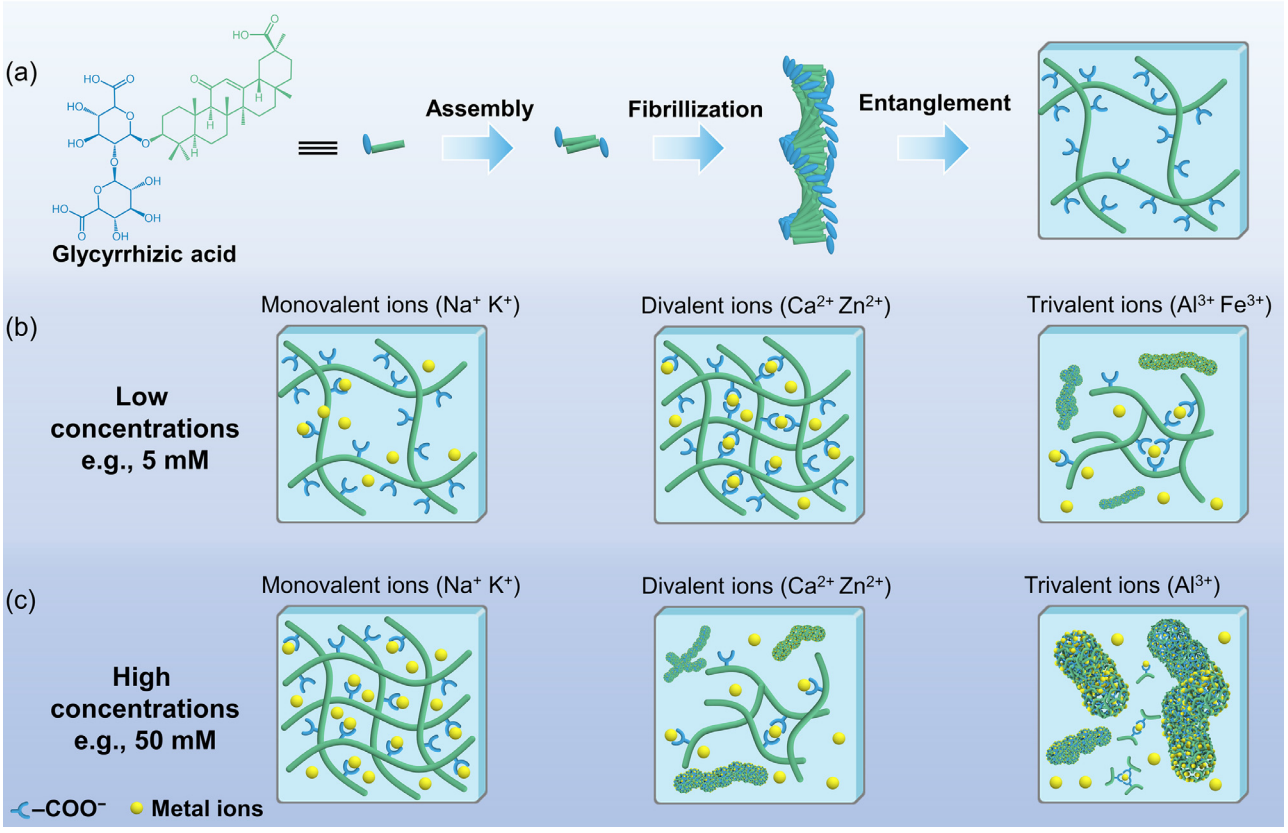

Fig. 8

Schematic illustration of metal ion-modulated GA supramolecular hydrogel networks.

in diglucuronic unit, and C–O stretching vibration, respectively [27,42]. At a metal ion concentration of 5 mM, only the C = C stretching band of GA-5Fe^{3+} and GA-5Al^{3+}moved to a lower wavenumber (1643 cm^{-1} for GA-5Fe^{3+}and 1653 cm^{-1} for GA-5Al^{3+}, respectively), and no significant changes were observed in the characteristic peaks of the other samples (Fig. S6). When the concentration of metal ions reached 50 mM (Fig. 7b), the main characteristic peaks of GA-50Na^{+} and GA-50K^{+} remained unchanged obviously as compared to pure GA (0 mM). In contrast, for GA-50Ca^{2+}, GA-50Zn^{2+}, and GA-50Al^{3+}, the C = O stretching band disappeared, and the C = C stretching band shifted to a lower wavenumber (1638 cm^{-1} for GA-50Ca^{2+}, 1636 cm^{-1} for GA-50Zn^{2+}, and 1640 cm^{-1} for GA-50Al^{3+}, respectively). Additionally, the intensity of the O–H stretching band, –CH$_3$ stretching band, and C–O stretching band diminished, especially for the GA-50Al^{3+}, suggesting a strong binding between GA and these polyvalent metal ions with relatively high concentrations. The FTIR results indicate that the monovalent metal ions (Na^{+} and K^{+}) bind weakly to GA, which shows no significant effect on the network structure of GA at low and high metal ion concentrations. While the polyvalent metal ions (Ca^{2+}, Zn^{2+}, and Al^{3+}) can bind heavily with the carboxylate of GA at high concentrations (e.g., 50 mM) and may disrupt the hydrophobic interactions of the triterpene fragments and the hydrogen bonds of the diglucuronic fragments, which leads to the collapse of GA fibrillar structure and thus an irregular and discrete aggregated network (Fig. S3j-l). This can be further supported by the XPS data. As can be seen, the results from the XPS survey spectra revealed the presence of corresponding metal species in the GA-M^{n+} samples (Fig. S7). Fig. 7a displayed the high-resolution XPS C 1 s spectra of GA-M^{n+}, featuring prominent peaks centered at binding energies near 284.8, 286.6, and 289.0 eV, which were assigned to C–C, C–O, O = C–O, respectively [64]. Pure GA, GA-50Na^{+}, and GA-50K^{+} exhibited similar XPS C 1 s spectra, while the peak intensities of C–C for GA-50Ca^{2+}, GA-50Zn^{2+}, and GA-50Al^{3+} were significantly reduced, resulting in a flatter overall peak shape and the less visible sites of C–O and O = C–O (Fig. 7a).

The binding energy (E_b) was calculated by density functional theory (DFT) with the aim of gaining further insights into the metal ions-carboxylate complexation. E_b represents the energy decrement associated with the process of metal ion-carboxylate binding, reflecting the efficacy of carboxylate binding by different metal ions. There are three carboxyl groups in the GA molecule, which refer to the carboxyl 1 (carboxyl group of glucuronic unit far from triterpene fragment, pKa=3.98), carboxyl 2 (carboxyl group of glucuronic unit linked to triterpene fragment, pKa=4.62), and carboxyl 3 (carboxyl group of triterpene fragment, pKa=5.17). The dissociation of GA does not occur at pH values lower than 2 [65]. At pH levels ranging from 2 to 3, the carboxyl 1 experiences dissociation. In the pH range of 3 to 4, the dissociations of both carboxyl 1 and 2 overlap. Furthermore, in the pH range of 4 to 5, the dissociation of all three carboxyl groups overlaps.

Only at pH values higher than 7, a fully deprotonated GA exists. The pH of GA-M^{n+} was approximately 4.0–4.1, at which all three carboxyls dissociate to varying degrees, and we chose the carboxyl 1 (pKa= 3.98) to calculate its binding energy to the metal ions (Fig. 7c). As depicted in Fig. 7c, the binding energy E_b followed the order of K^+ (0.66 eV) < Na^+ (0.88 eV) < Ca^{2+}(2.09 eV) < Zn^{2+} (4.44 eV) < Al^{3+} (6.97 eV) < Fe^{3+}(7.41 eV). Based on this observation, it can be inferred that as E_b increases progressively from K^+ to Fe^{3+}, the carboxylate binding process becomes increasingly efficient. This means that the polyvalent metal ions were more readily bound to the carboxyl groups of GA to form ionic bonding. In combination with the zeta potential results (Fig. 7d), it can be observed that the metal ions with higher valence and greater charge density possessed a greater capability to modulate the surface charge condition of GA. A higher valence corresponds to a more pronounced electrostatic screening effect, and as the concentration of metal ions increased (0–100 mM), the zeta potential values proceeded faster to 0, and in some cases even attained positive values (Al^{3+} and Fe^{3+}). The electrostatic screening effect is the cause of the significantly enhanced network strength of the GA hydrogels by Ca^{2+}, Zn^{2+}, and Al^{3+} at low concentrations (e.g., 5 mM), but by Na^+ and K^+at high concentrations (e.g., 50 mM). Nevertheless, for the polyvalent metal ions (Ca^{2+}, Zn^{2+}, and Al^{3+}) at high concentrations (e.g., 50 mM), the very strong cation-carboxylate complexation can lead to a fast and extensive aggregation, resulting in an unstable GA fibrillar structure and thereby the formation of large aggregates and clusters, which can hinder the development of well-formed and interconnected gel networks [66]. This is the reason why the GA-50Ca^{2+}, GA-50Zn^{2+}, and GA-50Al^{3+} showed an irregular and discrete aggregated network (Fig. S3j-l) and even the failure of GA-50Fe^{3+} to form a gel network (Fig. S4).

On the basis of these above-mentioned results, the schematic diagram of the GA-M^{n+} gel network structures showing the structural variations induced by different metal ions was proposed and depicted in Fig. 8. At lower concentrations of metal ions (e.g., 5 mM), the gel samples with the monovalent metal ions (Na^+ and K^+) exhibited similar fibrillar network structures to pure GA. The addition of the divalent (Ca^{2+} and Zn^{2+}) and trivalent metal ions (Al^{3+} and Fe^{3+}) led to a more tightly fibrillar structure of GA hydrogels due to their more pronounced electrostatic screening effect and thus the enhanced interfibrillar binding. At higher concentrations of metal ions (e.g., 50 mM), the fibrous network with monovalent metal ions (Na^+ and K^+) became more compact and ordered, whereas a discrete aggregated network structure was observed for both divalent (Ca^{2+} and Zn^{2+}) and trivalent (Al^{3+}) metal ions, especially for the GA-50Al^{3+}, which showed a particularly pronounced network aggregation and clustering.

4 Conclusions

In summary, we have found that the metal ions with different valence states and concentrations can largely tune the linear and nonlinear rheological properties and network structures of the natural GA supramolecular hydrogels. Monovalent metal ions (Na^+ and K^+) at low concentrations (e.g., 5 mM) have slight effects on the rheological and structural properties of GA hydrogels because of low binding affinity to GA. At high concentrations (e.g., 50 mM), these monovalent metal ions endow the GA hydrogel with a relatively more compact and ordered network structure to enhance the gel strength via electrostatic screening effects, which exhibits pronounced nonlinear rheological properties with a typical transition from elastic to viscous response. In contrast, polyvalent metal ions (Ca^{2+}, Zn^{2+}, and Al^{3+}), can significantly enhance the network strength of the hydrogel at low concentrations (e.g., 5 mM), which is attributed to their higher charge density and stronger binding with GA. Nonetheless, at high ion concentrations (e.g., 50 mM), the excessively strong cation-carboxylate complexation leads to an unstable GA fibrillar structure and thus the formation of discrete aggregated gel networks. As a result, the obtained GA-M^{n+}hydrogels display an irregular nonlinear rheological behavior and the lower resistance to large deformations.

The current study complements earlier works which reported that the addition of monovalent metal ions such as Na^+ can significantly increase the viscoelastic properties of GA supramolecular hydrogels [27,42,63]; however, there is a lack of understanding of how the monovalent metal ions affect the rheological and structural properties of GA hydrogels and whether the other types of metal ions have similar or different effects. Currently, we comprehensively investigated the influence of the incorporation of the metal ions with different valence states and concentrations on the linear and nonlinear rheological and network structures of GA hydrogels. The above-mentioned findings shown in this work enrich and deepen our understanding of the highly tunable rheological behavior and network structure of GA hydrogels, which provides a new perspective for the design and development of responsive natural LMWGs supramolecular hydrogels with controlled properties through the strategy of metal ion complexation. These supramolecular hydrogels with adjustable structural properties from natural edible bioactive building blocks (i.e., GA) are expected to find sustainable applications in food and biomedical fields, such as the use as active cargo delivery and release platform and as the template for advanced biomaterial designs.

Declaration of competing interest

The authors declare that they have no known competing financial interests or personal relationships that could have appeared to influence the work reported in this paper.

Data availability

Data will be made available on request.

CRediT authorship contribution statement

Xinke Yu: Investigation, Methodology, Formal analysis, Visualization, Writing – original draft. **Mengyue Xu:** Investigation, Methodology, Formal analysis. **Jiyang Cai:** Investigation, Methodology, Formal analysis. **Qing Li:** Formal analysis. **Yunyi Yang:** Formal analysis. **Zhili Wan:** Conceptualization, Methodology, Supervision, Project administration, Funding acquisition, Resources, Formal analysis, Writing – review & editing. **Xiaoquan Yang:** Conceptualization, Resources.

Acknowledgement

This work is financially supported by the National Natural Science Foundation of China (32172347), the Guangzhou Science and Technology Plan Project (202201010209), and the 111 Project (B17018).

Supplementary materials

Supplementary material associated with this article can be found, in the online version, at doi:10.1016/j.giant.2024.100240.

References

[1] P. Terech, R.G. Weiss, Low molecular mass gelators of organic liquids and the properties of their gels, Chem. Rev. 97 (1997) 3133–3160, doi:10.1021/cr9700282.

[2] L.A. Estroff, A.D. Hamilton, Water gelation by small organic molecules, Chem. Rev. 104 (2004) 1201–1218, doi:10.1021/cr0302049.

[3] A.R. Hirst, B. Escuder, J.F. Miravet, D.K. Smith, High-tech applications of self-assembling supramolecular nanostructured gel-phase materials: from regenerative medicine to electronic devices, Angew. Chem. Int. Ed. 47 (2008) 8002–8018, doi:10.1002/anie.200800022.

[4] J.W. Steed, Supramolecular gel chemistry: developments over the last decade, Chem. Commun. 47 (2011) 1379–1383, doi:10.1039/C0CC03293J.

[5] R.G. Weiss, The past, present, and future of molecular gels. What is the status of the field, and where is it going? J. Am. Chem. Soc. 136 (2014) 7519–7530, doi:10.1021/ja503363v.

[6] E.R. Draper, D.J. Adams, Low-molecular-weight gels: the state of the art, Chem 3 (2017) 390–410, doi:10.1016/j.chempr.2017.07.012.

[7] D.J. Adams, Personal perspective on understanding low molecular weight gels, J. Am. Chem. Soc. 144 (2022) 11047–11053, doi:10.1021/jacs.2c02096.

[8] D.J. Cornwell, D.K. Smith, Expanding the scope of gels – combining polymers with low-molecular-weight gelators to yield modified self-assembling smart materials with high-tech applications, Mater. Horiz. 2 (2015) 279–293, doi:10.1039/C4MH00245H.

[9] M.O.M. Piepenbrock, G.O. Lloyd, N. Clarke, J.W. Steed, Metal- and anion-binding supramolecular gels, Chem. Rev. 110 (2010) 1960–2004, doi:10.1021/cr9003067.

[10] J. Zheng, R. Fan, H. Wu, H. Yao, Y. Yan, J. Liu, L. Ran, Z. Sun, L. Yi, L. Dang, P. Gan, P. Zheng, T. Yang, Y. Zhang, T. Tang, Y. Wang, Directed self-assembly of herbal small molecules into sustained release hydrogels for treating neural inflammation, Nat. Commun. 10 (2019) 1604, doi:10.1038/s41467-019-09601-3.

[11] J. Wang, H. Zhao, W. Qiao, J. Cheng, Y. Han, X. Yang, Nanomedicine-cum-carrier by co-assembly of natural small products for synergistic enhanced antitumor with tissues protective actions, ACS Appl. Mater. Interfaces 12 (2020) 42537–42550, doi:10.1021/acsami.0c12641.

[12] H. Huang, W. Gong, X. Wang, W. He, Y. Hou, J. Hu, Self-assembly of naturally small molecules into supramolecular fibrillar networks for wound healing, Adv. Healthc. Mater. 11 (2022) 2102476, doi:10.1002/adhm.202102476.

[13] M.N. Asl, H. Hosseinzadeh, Review of pharmacological effects of glycyrrhiza sp. and its bioactive compounds, Phytother. Res. 22 (2008) 709–724, doi:10.1002/ptr.2362.

[14] B. Schröfelbauer, J. Raffetseder, M. Hauner, A. Wolkerstorfer, W. Ernst, O.H.J. Szolar, Glycyrrhizin, the main active compound in liquorice, attenuates pro-inflammatory responses by interfering with membrane-dependent receptor signalling, Biochem. J. 421 (2009) 473–482, doi:10.1042/BJ20082416.

[15] Z. Zhao, Y. Xiao, L. Xu, Y. Liu, G. Jiang, W. Wang, B. Li, T. Zhu, Q. Tan, L. Tang, H. Zhou, X. Huang, H. Shan, Glycyrrhizic acid nanoparticles as antiviral and anti-inflammatory agents for COVID-19 treatment, ACS Appl. Mater. Interfaces 13 (2021) 20995–21006, doi:10.1021/acsami.1c02755.

[16] Q. Li, Z. Wan, X. Yang, Glycyrrhizic acid: self-assembly and applications in multiphase food systems, Curr. Opin. Food Sci. 43 (2022) 107–113, doi:10.1016/j.cofs.2021.11.008.

[17] A. Saha, J. Adamcik, S. Bolisetty, S. Handschin, R. Mezzenga, Fibrillar networks of glycyrrhizic acid for hybrid nanomaterials with catalytic features, Angew. Chem. Int. Ed. 54 (2015) 5408–5412, doi:10.1002/anie.201411875.

[18] Y. Ma, J. Hao, K. Zhao, Y. Ju, J. Hu, Y. Gao, F. Du, Biobased polymeric surfactant: natural glycyrrhizic acid-appended homopolymer with multiple pH-responsiveness, J. Colloid Interface Sci. 541 (2019) 93–100, doi:10.1016/j.jcis.2019.01.088.

[19] Y. Gao, K. Zhao, X. Yu, Z. Li, T. Wu, C. Zhang, F. Du, J. Hu, Multiple modulations of supramolecular assemblies from a natural triterpenoid-tailored bipyridinium amphiphile, J. Colloid Interface Sci. 584 (2021) 92–102, doi:10.1016/j.jcis.2020.09.125.

[20] L. Zhao, H. Zhang, Z. Guo, X. Yu, X. Jiao, M.H. Li, J. Hu, Natural glycyrrhizic acid-tailored homogeneous conductive polyaniline hydrogel as a flexible strain sensor, ACS Appl. Mater. Interfaces 14 (2022) 51394–51403, doi:10.1021/acsami.2c16129.

[21] W. Liu, Z. Li, Z. Wang, Z. Huang, C. Sun, S. Liu, Y. Jiang, H. Yang, Functional system based on glycyrrhizic acid supramolecular hydrogel: toward polymorph control, stabilization, and controlled release, ACS Appl. Mater. Interfaces 15 (2023) 7767–7776, doi:10.1021/acsami.2c19903.

[22] Z. Wan, Y. Sun, L. Ma, X. Yang, J. Guo, S. Yin, Responsive emulsion gels with tunable properties formed by self-assembled nanofibrils of natural saponin glycyrrhizic acid for oil structuring, J. Agric. Food Chem. 65 (2017) 2394–2405, doi:10.1021/acs.jafc.6b05242.

[23] Q. Li, M. Xu, J. Xie, E. Su, Z. Wan, L.M.C. Sagis, X. Yang, Large amplitude oscillatory shear (LAOS) for nonlinear rheological behavior of heterogeneous emulsion gels made from natural supramolecular gelators, Food Res. Int. 140 (2021) 110076, doi:10.1016/j.foodres.2020.110076.

[24] R. Du, Y. Liu, Q. Li, J. Chen, X. Yu, Z. Wan, X. Yang, All-natural, plant-based nanofibrils from citrus fiber and glycyrrhizic acid for stabilization of edible emulsion gels, ACS Sustain. Chem. Eng. 11 (2023) 12230–12242, doi:10.1021/acssuschemeng.3c00704.

[25] Z. Wan, Y. Sun, L. Ma, F. Zhou, J. Guo, S. Hu, X. Yang, Long-lived and thermoresponsive emulsion foams stabilized by self-assembled saponin nanofibrils and fibrillar network, Langmuir 34 (2018) 3971–3980, doi:10.1021/acs.langmuir.8b00128.

[26] L. Ma, Q. Li, Z. Du, E. Su, X. Liu, Z. Wan, X. Yang, A natural supramolecular saponin hydrogelator for creation of ultrastable and thermostimulable food-grade foams, Adv. Mater. Interfaces 6 (2019) 1900417, doi:10.1002/admi.201900417.

[27] E. Su, Q. Li, M. Xu, Y. Yuan, Z. Wan, X. Yang, B.P. Binks, Highly stable and thermo-responsive gel foams by synergistically combining glycyrrhizic acid nanofibrils and cellulose nanocrystals, J. Colloid Interface Sci. 587 (2021) 797–809, doi:10.1016/j.jcis.2020.11.039.

[28] Q. Li, X. Yu, S. Zhang, M. Xu, Y. Yang, Z. Wan, X. Yang, All-natural, robust, and pH-responsive glycyrrhizic acid-based double network hydrogels for controlled nutrient release, ACS Appl. Mater. Interfaces 15 (2023) 43633–43647, doi:10.1021/acsami.3c10407.

[29] Q. Li, S. Zhang, R. Du, Y. Yang, Y. Liu, Z. Wan, X. Yang, Injectable self-healing adhesive natural Glycyrrhizic acid bioactive hydrogel for bacteria-infected wound healing, ACS Appl. Mater. Interfaces 15 (2023) 17562–17576, doi:10.1021/acsami.2c23231.

[30] M.C. Nolan, A.M.F. Caparrós, B. Dietrich, M. Barrow, E.R. Cross, M. Bleuel, S.M. King, D.J. Adams, Optimising low molecular weight hydrogels for automated 3D printing, Soft Matter 13 (2017) 8426–8432, doi:10.1039/C7SM01694H.

[31] C.C. Piras, P. Slavik, D.K. Smith, Self-assembling supramolecular hybrid hydrogel beads, Angew. Chem. Int. Ed. 59 (2020) 853–859, doi:10.1002/anie.201911404.

[32] J. Raeburn, C. Mendoza-Cuenca, B.N. Cattoz, M.A. Little, A.E. Terry, A. Zamith Cardoso, P.C. Griffiths, D.J. Adams, The effect of solvent choice on the gelation and final hydrogel properties of Fmoc–diphenylalanine, Soft Matter 11 (2015) 927–935, doi:10.1039/C4SM02256D.

[33] S. Xian, M.J. Webber, Temperature-responsive supramolecular hydrogels, J. Mater. Chem. B 8 (2020) 9197–9211, doi:10.1039/D0TB01814G.

[34] D.J. Cornwell, O.J. Daubney, D.K. Smith, Photopatterned multidomain gels: multi-component self-assembled hydrogels based on partially self-sorting 1,3:2,4-dibenzylidene-D-sorbitol derivatives, J. Am. Chem. Soc. 137 (2015) 15486–15492, doi:10.1021/jacs.5b09691.

[35] Q. Lin, T. Lu, X. Zhu, T. Wei, H. Li, Y. Zhang, Rationally introduce multi-competitive binding interactions in supramolecular gels: a simple and efficient approach to develop multi-analyte sensor array, Chem. Sci. 7 (2016) 5341–5346, doi:10.1039/C6SC00955G.

[36] W. Weng, J.B. Beck, A.M. Jamieson, S.J. Rowan, Understanding the mechanism of gelation and stimuli-responsive nature of a class of metallo-supramolecular gels, J. Am. Chem. Soc. 128 (2006) 11663–11672, doi:10.1021/ja063408q.

[37] H. McEwen, E.Y. Du, J.P. Mata, P. Thordarson, A.D. Martin, Tuning hydrogels through metal-based gelation triggers, J. Mater. Chem. B 5 (2017) 9412–9417, doi:10.1039/C7TB02140B.

[38] G. Picci, C. Caltagirone, A. Garau, V. Lippolis, J. Milia, J.W. Steed, Metal-based gels: synthesis, properties, and applications, Coord. Chem. Rev. 492 (2023) 215225, doi:10.1016/j.ccr.2023.215225.

[39] K. McAulay, P.A. Ucha, H. Wang, A.M. Fuentes-Caparrós, L. Thomson, O. Maklad, N. Khunti, N. Cowieson, M. Wallace, H. Cui, R.J. Poole, A. Seddon, D.J. Adams, Controlling the properties of the micellar and gel phase by varying the counterion in functionalised-dipeptide systems, Chem. Commun. 56 (2020) 4094–4097, doi:10.1039/D0CC01252A.

[40] M.A. Ramin, K.R. Sindhu, A. Appavoo, K. Oumzil, M.W. Grinstaff, O. Chassande, P. Barthélémy, Cation tuning of supramolecular gel properties: a new paradigm for sustained drug delivery, Adv. Mater. 29 (2017) 1605227, doi:10.1002/adma.201605227.

[41] P. Sharma, H. Kaur, S. Roy, Inducing differential self-assembling behavior in ultrashort peptide hydrogelators using simple metal salts, Biomacromolecules 20 (2019) 2610–2624, doi:10.1021/acs.biomac.9b00416.

[42] Y. Qian, Y. Zheng, J. Jin, X. Wu, K. Xu, M. Dai, Q. Niu, H. Zheng, X. He, J. Shen, Immunoregulation in diabetic wound repair with a photoenhanced glycyrrhizic acid hydrogel scaffold, Adv. Mater. 34 (2022) 2200521, doi:10.1002/adma.202200521.

[43] I.M. Tucker, A. Burley, R.E. Petkova, S.L. Hosking, J. Penfold, R.K. Thomas, P.X. Li, J.R.P. Webster, R. Welbourn, J. Doutch, Adsorption and self-assembly properties of the plant based biosurfactant, Glycyrrhizic acid, J. Colloid Interface Sci. 598 (2021) 444–454, doi:10.1016/j.jcis.2021.03.101.

[44] W.H. Shih, W.Y. Shih, S.I. Kim, J. Liu, I.A. Aksay, Scaling behavior of the elastic properties of colloidal gels, Phys. Rev. A 42 (1990) 4772–4779, doi:10.1103/PhysRevA.42.4772.

[45] N.M. Wereley, A. Chaudhuri, J.H. Yoo, S. John, S. Kotha, A. Suggs, R. Radhakrishnan, B.J. Love, T.S. Sudarshan, Bidisperse magnetorheological fluids using Fe particles at nanometer and micron scale, J. Intell. Mater. Syst. Struct. 17 (2006) 393–401, doi:10.1177/1045389X06056953.

[46] F.K.G. Schreuders, L.M.C. Sagis, I. Bodnár, R.M. Boom, A.J. van der Goot, Nonlinear rheology reveals the importance of elasticity in meat and meat analogues, Sci. Rep. 12 (2022) 1334, doi:10.1038/s41598-021-04478-z.

[47] R.H. Ewoldt, A.E. Hosoi, G.H. McKinley, New measures for characterizing nonlinear viscoelasticity in large amplitude oscillatory shear, J. Rheol. 52 (2008) 1427–1458, doi:10.1122/1.2970095.

[48] R.H. Ewoldt, P. Winter, J. Maxey, G.H. McKinley, Large amplitude oscillatory shear of pseudoplastic and elastoviscoplastic materials, Rheol. Acta 49 (2010) 191–212, doi:10.1007/s00397-009-0403-7.

[49] F. Neese, The ORCA program system, WIREs Comput. Mol. Sci. 2 (2012) 73–78, doi:10.1002/wcms.81.

[50] F. Neese, Software update: the ORCA program system, version 4.0, WIREs Comput. Mol. Sci. 8 (2018) e1327, doi:10.1002/wcms.1327.

[51] F. Neese, F. Wennmohs, U. Becker, C. Riplinger, The ORCA quantum chemistry program package, J. Chem. Phys. 152 (2020) 224108, doi:10.1063/5.0004608.

[52] F. Neese, Software update: the ORCA program system—version 5.0, WIREs Comput. Mol. Sci. 12 (2022) e1606, doi:10.1002/wcms.1606.

[53] S. Grimme, S. Ehrlich, L. Goerigk, Effect of the damping function in dispersion corrected density functional theory, J. Comput. Chem. 32 (2011) 1456–1465, doi:10.1002/jcc.21759.

[54] K. Momma, F. Izumi, VESTA 3 for three-dimensional visualization of crystal, volumetric and morphology data, J. Appl. Cryst. 44 (2011) 1272–1276, doi:10.1107/S0021889811038970.

[55] S. Lu, Y. Yang, J. Yao, Z. Shao, X. Chen, Exploration of the nature of a unique natural polymer-based thermosensitive hydrogel, Soft Matter 12 (2015) 492–499, doi:10.1039/C5SM01947H.

[56] K. Hyun, M. Wilhelm, C.O. Klein, K.S. Cho, J.G. Nam, K.H. Ahn, S.J. Lee, R.H. Ewoldt, G.H. McKinley, A review of nonlinear oscillatory shear tests: analysis and application of large amplitude oscillatory shear (LAOS), Prog. Polym. Sci. 36 (2011) 1697–1753, doi:10.1016/j.progpolymsci.2011.02.002.

[57] M.H. Tunick, D.L. Van Hekken, Rheology and texture of commercial queso fresco cheeses made from raw and pasteurized milk, J. Food Qual. 33 (2010) 204–215, doi:10.1111/j.1745-4557.2010.00331.x.

[58] S. Precha-Atsawanan, D. Uttapap, L.M.C. Sagis, Linear and nonlinear rheological behavior of native and debranched waxy rice starch gels, Food Hydrocolloids 85 (2018) 1–9, doi:10.1016/j.foodhyd.2018.06.050.

[59] M.R.B. Mermet-Guyennet, J. Gianfelice de Castro, M. Habibi, N. Martzel, M.M. Denn, D. Bonn, LAOS: the strain softening/strain hardening paradox, J. Rheol. 59 (2015) 21–32, doi:10.1122/1.4902000.

[60] O.C. Duvarci, G. Yazar, J.L. Kokini, The comparison of LAOS behavior of structured food materials (suspensions, emulsions and elastic networks), Trends Food Sci. Technol. 60 (2017) 2–11, doi:10.1016/j.tifs.2016.08.014.

[61] S. Tarashi, H. Nazockdast, A. Bandegi, S. Shafaghsorkh, G. Sodeifian, R. Foudazi, Large amplitude oscillatory shear behavior of thermoresponsive hydrogels: single versus double network, J. Rheol. 67 (2023) 15–33, doi:10.1122/8.0000457.

[62] F.K.G. Schreuders, L.M.C. Sagis, I. Bodnár, P. Erni, R.M. Boom, A.J. van der Goot, Small and large oscillatory shear properties of concentrated proteins, Food Hydrocolloids 110 (2021) 106172, doi:10.1016/j.foodhyd.2020.106172.

[63] L. Ma, P. Bertsch, Z. Wan, X. Yang, P. Fischer, Synergistic effect of glycyrrhizic acid and cellulose nanocrystals for oil-water interfacial stabilization, Food Hydrocolloids 120 (2021) 106888, doi:10.1016/j.foodhyd.2021.106888.

[64] Z. Huang, H. Xie, T. Hu, J. Zeng, X. Tian, Z. Wu, Preparing bright Monascus yellow pigments by loading quercetin-Sn(II)- albumin –chitosan: enhanced stability and bioactivity, Food Hydrocoll 142 (2023) 108776, doi:10.1016/j.foodhyd.2023.108776.

[65] C.X. Zeng, Q. Hu, Determination of the polyacid dissociation constants of glycyrrhizic acid, Indian J. Chem. - Sect. Inorg. Phys. Theor. Anal. Chem. 47 (2008) 71–74 http://nopr.niscpr.res.in/handle/123456789/555.

[66] R. Du, Y. Hu, R. Hübner, J.O. Joswig, X. Fan, K. Schneider, A. Eychmüller, Specific ion effects directed noble metal aerogels: versatile manipulation for electrocatalysis and beyond, Sci. Adv. 5 (2019) eaaw4590, doi:10.1126/sciadv.aaw4590.